

https://dspace.org/

Direct synthesis of PtNi coated with Ni3B for efficient electrochemical hydrogen evolution from seawater

X Yang; Y Xiao; Fei Yu; Wen-Ying Zhao; Kenneth Ozoemena ...

ROYAL SOC CHEMISTRY
https://hdl.handle.net/10539/46663
WOS

Downloaded from a DSpace repository. https://dspace.org/

ChemComm

COMMUNICATION

View Article Online
View Journal | View Issue

Published on 06 December 2024. Downloaded by University of the Witwatersrand on 7/30/2025 2:13:24 PM.

Check for updates

Cite this: *Chem. Commun.*, 2025, **61**, 760

Received 24th August 2024,
Accepted 4th December 2024

DOI: 10.1039/d4cc04333b

rsc.li/chemcomm

Direct synthesis of PtNi coated with Ni_3B for efficient electrochemical hydrogen evolution from seawater†

Xiong Yang,[a] Yu-Xuan Xiao,*[b] Fei Yu,[a] Wen-Ying Zhao,[a] Ling Shen,[a] Jie Ying,[b] Song Zhang,[a] Kenneth I. Ozoemena,[c] Christoph Janiak[d] and Xiao-Yu Yang*[ae]

The design of a protective electron-rich surface is an ideal route to enhance the performance of catalysts. Due to the higher work function of Ni_3B, facile-directed electron transport occurs from PtNi to Ni_3B to enrich electron density on the surface of the Ni_3B shell. This process increases hydrogen adsorption–desorption kinetics and mitigates Cl^- corrosion.

Electrolysis of seawater for hydrogen production, as a future option of green energy, has been paid attention in national plans, scientific research and industrial interest.[1–3] However, many issues need to be addressed such as serious corrosion and easy catalyst deactivation caused by the abundance of chloride ions in seawater with metal chloride/hydroxide formation (eqn (1)–(3)).[4–6] One win–win technique is heteroatom (P, S, O, B, and N) incorporation into the metal catalyst, which enables avoiding Cl^- adsorption and enhances the durability of Pt-based catalysts because of their anion-rich design promoting water affinity and H* desorption to benefit seawater splitting.[7]

$$Pt + Cl^- \rightarrow PtCl_{ads} + e^- \quad (1)$$

$$PtCl_{ads} + Cl^- \rightarrow PtCl_x^- \quad (2)$$

$$PtCl_x + OH^- \rightarrow Pt(OH)_x + Cl^- \quad (3)$$

Nanostructured PtNi is considered as one of the best catalysts for the hydrogen evolution reaction (HER) of water electrolysis.[8,9] The application of PtNi catalysts in seawater electrolysis for efficient hydrogen could be predicted, although Ni shows poor stability during electrocatalytic seawater splitting.[10] However, it has to be pointed out that the excess doping of P, S, O, B, and N onto the Ni/Pt surface would reduce the exposed metal sites and decrease its electrocatalytic activity.[11] Ni_3B is a stable compound with a high metallic conductivity owing to delocalized electrons.[12,13] More importantly, the presence of Ni in both alloys could improve the lattice match and interface fusion between PtNi and Ni_3B.[14] Very interestingly, the work function of Ni_3B is higher than that of PtNi, which is available to direct electron transfer for improvement of both the electrocatalytic activity and stability in seawater.[15] Moreover, compared with post-synthesis such as post-doping, modifying and treatment, the direct-synthesis of a PtNi–NiB nanostructure is mostly preferred.

In this work, a facile direct synthesis at room temperature in an open system of PtNi coated with Ni_3B (denoted as Pt_3Ni_{2-3x}@$(Ni_3B)_x$) has been developed. Experimental characterizations and theoretical calculations suggested the existence of directed electron transfer and enhanced Cl^- resistance in Pt_3Ni_{2-3x}@$(Ni_3B)_x$. Benefiting from the advantages of Ni_3B: (i) the intrinsic stability of Ni_3B can serve as a natural parclose for PtNi to avoid the corrosive Cl^-; (ii) the intermetallic properties of Ni_3B can accelerate the unfavorable water dissociation step of PtNi for promoted electrocatalytic kinetics; (iii) the gap of the work function can facilitate a directed electron transfer from PtNi to Ni_3B for both an improved electrocatalytic step and enhanced surface electronegativity. Pt_3Ni_{2-3x}@$(Ni_3B)_x$ displays superior performance in catalyzing the HER in an aqueous alkaline medium (1 mol L^{-1} KOH) and alkaline seawater (1 mol L^{-1} KOH + 3.5 wt% NaCl) with high durability.

A schematic representation of the method used to construct Pt_3Ni_{2-3x}@$(Ni_3B)_x$ is shown in Fig. 1a. In this route, the precursor of the catalyst was generated by the reduction of H_2PtCl_6 and $NiCl_2$ reduced by $NaBH_4$ to rapidly form PtNi nanowires. Then, with the prolonging of the reaction time, a layer of Ni_3B was formed and

[a] *State Key Laboratory of Silicate Materials for Architectures & State Key Laboratory of Advanced Technology for Materials Synthesis and Processing & School of Chemistry, Chemical Engineering and Life Sciences & Laoshan Laboratory & School of Materials Science and Engineering & International School of Materials Science and Engineering, Wuhan University of Technology, Wuhan, 430070, China. E-mail: xyyang@whut.edu.cn*

[b] *School of Chemical Engineering and Technology, Sun Yat-sen University, Zhuhai, 519082, China. E-mail: xiaoyx63@mail.sysu.edu.cn*

[c] *Molecular Sciences Institute, School of Chemistry, University of the Witwatersrand, Private Bag 3, Johannesburg 2050, South Africa*

[d] *Institut für Anorganische Chemie und Strukturchemie, Heinrich-Heine-Universität Düsseldorf, Düsseldorf, 40204, Germany*

[e] *National Energy Key Laboratory for New Hydrogen-Ammonia Energy Technologies, Foshan Xianhu Laboratory, Foshan 528200, P. R. China*

† Electronic supplementary information (ESI) available. See DOI: https://doi.org/10.1039/d4cc04333b

This journal is © The Royal Society of Chemistry 2025

Published on 06 December 2024. Downloaded by University of the Witwatersrand on 7/30/2025 2:13:24 PM.

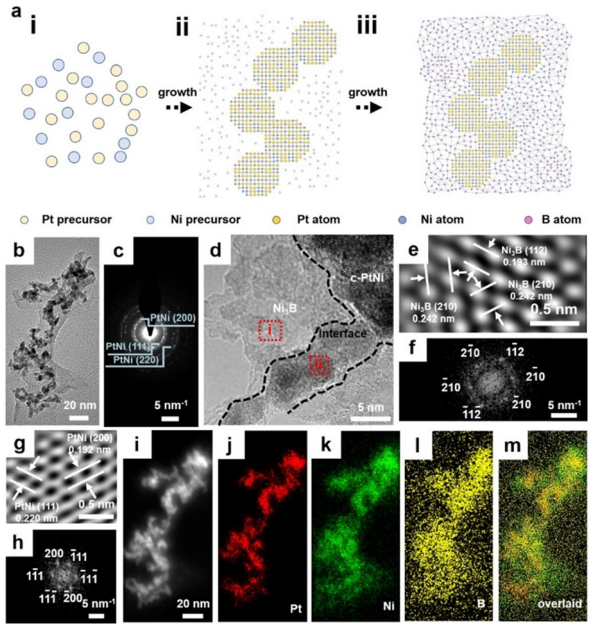


Fig. 1 (a) Illustration of the formation of the $Pt_3Ni_{2-3x}@(Ni_3B)_x$. (b) Low magnification TEM images and (c) electron diffraction pattern of $Pt_3Ni_{2-3x}@(Ni_3B)_x$. (d) HRTEM image of $Pt_3Ni_{2-3x}@(Ni_3B)_x$. Lattice fringes and corresponding FFT results of (e) and (f) Ni_3B and (g) and (h) PtNi corresponding to area i and ii in Fig. 1(d), respectively. (i) HAADF-STEM image of $Pt_3Ni_{2-3x}@(Ni_3B)_x$. EDX elemental mapping results of (j) Pt, (k) Ni, (l) B, and (m) overlaid color mapping for $Pt_3Ni_{2-3x}@(Ni_3B)_x$.

coated on the PtNi network. The morphology and content of the electrocatalysts could be regulated by controlling the ratio of Pt and Ni precursors during synthesis, as shown by the SEM (Fig. S1–S4, ESI†) and ICP-AES (Table S1, ESI†) results, which indicate that surplus Ni^{2+} would result in an increase of Ni_3B coating. Transmission electron microscopy (TEM) was conducted to further explore the morphology of $Pt_3Ni_{2-3x}@(Ni_3B)_x$. Compared to the network structure of Pt_3Ni (Fig. S5, ESI†), the TEM images of $Pt_3Ni_{2-3x}@(Ni_3B)_x$ show an obvious core–shell structure (Fig. 1d and Fig. S6, ESI†).

The fast Fourier transform (FFT) result of $Pt_3Ni_{2-3x}@(Ni_3B)_x$ contains a set of diffraction rings assignable to the (111), (220) and (200) planes of face-centered cubic (fcc) PtNi (Fig. 1c). Notably, high-resolution transmission electron microscopy (HRTEM, Fig. 1d) further reveals a partially crystalline structure of $Pt_3Ni_{2-3x}@(Ni_3B)_x$. The HRTEM (Fig. S7, ESI†) and the inverse Fourier transformation (IFT) image (Fig. 1e) of area i in the coating reveal the lattice spacings of 0.242 nm and 0.193 nm, which are consistent with the (210) and (112) planes of Ni_3B. Meanwhile, the FFT image belonging to area i shows the diffraction spots of the {210} and {112} planes of Ni_3B (Fig. 1f). The IFT image of area ii is also shown in Fig. 1g. It can be seen that the lattice spacings of the high crystallinity core in $Pt_3Ni_{2-3x}@(Ni_3B)_x$ are 0.220 nm and 0.192 nm, which are consistent with the (111) and (200) planes of fcc PtNi alloy. The FFT image of region ii also contains a set of diffraction rings assignable to the {111} and {200} planes in Fig. 1h, demonstrating the periodic structure and good crystallinity of PtNi. High angle annular dark-field detector (STEM-HAADF) imaging shows the specific outline of the inner PtNi without the imaging of the outer Ni_3B coating, which could be ascribed to the low crystallinity of the thin Ni_3B layers with few lattices to form the diffraction (Fig. 1i). The energy-dispersive X-ray elemental mappings of this heterophase structure clearly shows that Pt is homogeneously distributed along the networks while both Ni and B are distributed on the whole $Pt_3Ni_{2-3x}@(Ni_3B)_x$, further confirming the core–shell structure of $Pt_3Ni_{2-3x}@(Ni_3B)_x$ (Fig. 1j–m).

Fig. 2 shows more detailed structural characterizations of $Pt_3Ni_{2-3x}@(Ni_3B)_x$. As shown in Fig. 2a, the X-ray diffraction (XRD) peaks match well with fcc PtNi.[16,17] Note that the diffraction peak corresponding to Ni_3B is absent in the XRD patterns, possibly due to the short-range ordered crystallinity of the Ni_3B coating.[18] When the as-obtained $Pt_3Ni_{2-3x}@(Ni_3B)_x$ was further annealed under the protection of argon at 300 °C, the XRD peaks of Ni_3B become apparent, which illustrates the relatively low crystallinity of the Ni_3B (Fig. S8, ESI†). The surface areas and porosities were measured by N_2 physisorption isotherms (Fig. 2b). The Brunauer–Emmett–Teller (BET) surface area of $Pt_3Ni_{2-3x}@(Ni_3B)_x$ reaches a remarkable 169 $m^2\ g^{-1}$, which is rare in metal materials (Table S2, ESI†). Based on this, the high surface area can offer more active sites and improved catalytic activity.[19] Fig. S9 (ESI†) shows the pore size distribution results, which indicates a mesoporous structure for all samples.

As shown in Fig. 2c, the work functions (Φ) were tested by ultraviolet photoelectron spectroscopy (UPS), following the trends of Φ ($Pt_3Ni_{2-3x}@(Ni_3B)_x$) $\approx$ Φ ($Pt_2Ni_{3-3x}@(Ni_3B)_x$) $>$ Φ (Pt networks) $>$ Φ (Pt_3Ni networks). Considering that the work function is defined as the energy required for an electron from the Fermi level to escape from the metal in a potential well of depth Φ (see ESI†), electrons would transfer from PtNi to the Ni_3B coating. To further confirm the directed electron transfer, X-ray photoelectron spectroscopy (XPS) studies were conducted

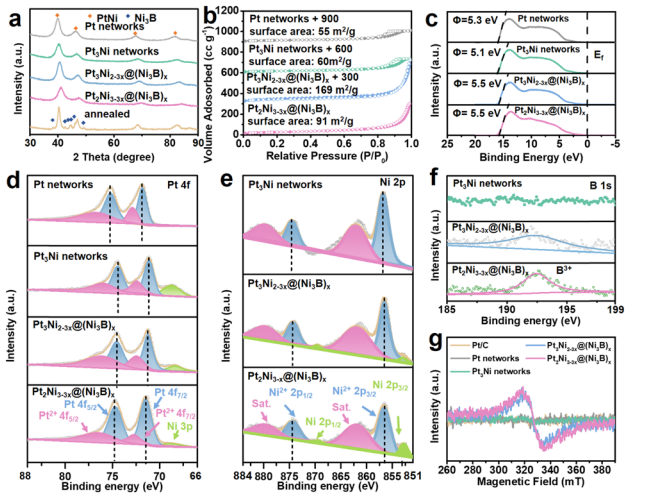


Fig. 2 (a) XRD patterns of the Pt networks, Pt_3Ni networks, $Pt_3Ni_{2-3x}@(Ni_3B)_x$, $Pt_2Ni_{3-3x}@(Ni_3B)_x$ and annealed $Pt_3Ni_{2-3x}@(Ni_3B)_x$. (b) Nitrogen physisorption isotherms (77 K) and (c) UPS spectra of the Pt networks, Pt_3Ni networks, $Pt_3Ni_{2-3x}@(Ni_3B)_x$, and $Pt_2Ni_{3-3x}@(Ni_3B)_x$. XPS spectra of (d) Pt 4f for the Pt networks, Pt_3Ni networks, $Pt_3Ni_{2-3x}@(Ni_3B)_x$, and $Pt_2Ni_{3-3x}@(Ni_3B)_x$, and (e) Ni 2p and (f) B 1s for the Pt_3Ni networks, $Pt_3Ni_{2-3x}@(Ni_3B)_x$, and $Pt_2Ni_{3-3x}@(Ni_3B)_x$. (g) ESR spectra of the Pt/C, Pt networks, Pt_3Ni networks, $Pt_3Ni_{2-3x}@(Ni_3B)_x$, and $Pt_2Ni_{3-3x}@(Ni_3B)_x$.

Published on 06 December 2024. Downloaded by University of the Witwatersrand on 7/30/2025 2:13:24 PM.

to explore the chemical states and structure (Fig. S10–S12, ESI†). The Pt 4f XPS spectra in Fig. 2d reveal that the Pt $4f_{7/2}$ peaks of the Pt_3Ni network (71.1 eV) are shifted to lower binding energies than that of the Pt networks (71.8 eV) (Table S3, ESI†), clearly illustrating electron migration from Ni to Pt owing to the difference of electronegativity between Ni (1.8) and Pt (2.2). Notably, the Pt $4f_{7/2}$ binding energies of these materials follow the sequence of $Pt_2Ni_{3-3x}@(Ni_3B)_x$ (71.5 eV) > $Pt_3Ni_{2-3x}@(Ni_3B)_x$ (71.3 eV) > Pt_3Ni networks (71.1 eV), revealing electron transfer from Pt to Ni_3B. Furthermore, $Pt_3Ni_{2-3x}@(Ni_3B)_x$ and $Pt_2Ni_{3-3x}@(Ni_3B)_x$ are shown in Fig. 2e. In contrast to Pt_3Ni networks (856.8 eV), the Ni 2p binding energies of $Pt_3Ni_{2-3x}@(Ni_3B)_x$ (856.6 eV) and $Pt_2Ni_{3-3x}@(Ni_3B)_x$ (856.5 eV) display negative shifts as a consequence of electron transport from Pt to Ni_3B. Moreover, metallic Ni $2p_{3/2}$ was absent in Pt_3Ni, due to Ni oxidated by the oxygen adsorbed on the surface of Pt_3Ni. The presence of metallic Ni $2p_{3/2}$ in $Pt_3Ni_{2-3x}@(Ni_3B)_x$ and $Pt_2Ni_{3-3x}@(Ni_3B)_x$ may come from the high oxidation resistance owing to the directed electron transfer. In addition, the stronger peak with 192.4 eV can be clearly observed for the B^{3+} spectra of $Pt_3Ni_{2-3x}@(Ni_3B)_x$ and $Pt_2Ni_{3-3x}@(Ni_3B)_x$ compared to that of the Pt_3Ni networks, suggesting the incorporation of B with the increase of Ni content during the preparation (Fig. 2f).[20,21] Electron spin resonance (ESR) measurements were also carried out to probe the unpaired electrons in $Pt_3Ni_{2-3x}@(Ni_3B)_x$ (Fig. 2g). Stronger single Lorentzian line signals can be observed for the spectra of $Pt_3Ni_{2-3x}@(Ni_3B)_x$ and $Pt_2Ni_{3-3x}@(Ni_3B)_x$ compared to that of the Pt_3Ni networks, suggesting that the Ni_3B composites possess a higher content of unpaired electrons as a result of the electron transport between PtNi and Ni_3B.[22]

The data in Fig. 3a and d and Fig. S13 (ESI†) clearly show that the HER activity follows the sequence of $Pt_3Ni_{2-3x}@(Ni_3B)_x$ > $Pt_2Ni_{3-3x}@(Ni_3B)_x$ > Pt_3Ni networks > Pt/C > Pt networks > Ni_3B. A summary of the overpotentials to drive a current density of 10 mA cm^{-2} (denoted as η_{10}) in different electrolytes is given in Fig. 3b, Fig. 3e and Table S4 (ESI†). $Pt_3Ni_{2-3x}@(Ni_3B)_x$ displays remarkable HER activities with only 19 mV and 16 mV of overpotential in alkaline media and alkaline seawater, respectively, which is much superior to those of Pt/C, Pt networks and Ni_3B. The results of the HER turnover frequencies (TOF) demonstrate the superior intrinsic activity of $Pt_3Ni_{2-3x}@(Ni_3B)_x$ (see Fig. S16, ESI† and a detailed description).[23] To investigate the catalytic mechanism of the HER, Tafel slopes were acquired by fitting the experimental data with the Butler–Volmer equation (Fig. 3c and f). $Pt_3Ni_{2-3x}@(Ni_3B)_x$ displays Tafel slopes of 21 mV dec^{-1} and 27 mV dec^{-1} in alkaline media and alkaline seawater, respectively. Note that the Tafel slope values of 120, 40 and 30 mV dec^{-1} correspond to the Volmer, Heyrovsky and Tafel reactions of the catalysts, respectively.[24] Thus, both the rate-determining steps on $Pt_3Ni_{2-3x}@(Ni_3B)_x$ in alkaline media and alkaline seawater are the Tafel step (2Pt–H → H_2 + 2Pt). The electrochemical impedance spectroscopy (EIS) and comparison of overpotential and Tafel slopes demonstrates the ideal potential of the HER in alkaline seawater (see Fig. S17, S18 and a detailed description, ESI†). To evaluate the durability and investigate the Cl^- corrosion resistance of the catalysts, the chronopotentiometry technique was applied in alkaline media (Fig. 3g) and alkaline seawater (Fig. 3h). The η_{10} values of the Pt/C, Pt_3Ni networks, and $Pt_3Ni_{2-3x}@(Ni_3B)_x$ increase by 217, 146 and 54 mV, after 20 hours in a chronoamperometric test in alkaline media, which indicates that $Pt_3Ni_{2-3x}@(Ni_3B)_x$ has excellent stability for the HER. Meanwhile, the η_{10} values of the Pt/C, Pt_3Ni networks, and $Pt_3Ni_{2-3x}@(Ni_3B)_x$ increase by 280, 274 and 56 mV, after 20 hours in a chronoamperometric test in alkaline seawater. Compared to the obvious decay of the Pt/C and Pt_3Ni networks in the chronoamperometric test with the presence of Cl^-, the similar stability of $Pt_3Ni_{2-3x}@(Ni_3B)_x$ in both of the electrolytes indicates the higher Cl^- corrosion resistance. The chronopotentiometry under the current density of 100 mA cm^{-2} in alkaline seawater, the zeta potential and the corresponding analysis of the dissolution of Pt and Ni indicate the superior stability of $Pt_3Ni_{2-3x}@(Ni_3B)_x$ (see Fig. S19, S20 and a detailed description, ESI†).

To elucidate the inherent relationship between the electronic structure and the excellent electrocatalytic HER performance of $Pt_3Ni_{2-3x}@(Ni_3B)_x$, density functional theory (DFT) calculations were performed (Fig. S21 and S22, ESI†).[25] As shown in Fig. 4a, $Pt_3Ni_{2-3x}@(Ni_3B)_x$ has a more negative water adsorption Gibbs free energy (ΔG_{w^*}) of −0.09 eV compared to that of Ni (0.04 eV), Pt (0.09 eV) and Pt_3Ni networks (0.21 eV), indicating the better performance to adsorb the water for a fast water dissociation. Moreover, the lower hydrogen adsorption Gibbs free energy (ΔG_{H^*}) of $Pt_3Ni_{23x}@(Ni_3B)_x$ (−0.24 eV) compared to the contrasted catalysts (Ni: −0.47 eV; Pt: −0.34 eV; Pt_3Ni: −0.56 eV) contributes to a better hydrogen desorption capability. Thereby, faster water dissociation and the more appropriate adsorption/desorption of H give $Pt_3Ni_{2-3x}@(Ni_3B)_x$ a better HER performance. To further investigate the effect of Cl^- on the catalysts in seawater, the Cl* adsorption calculation was conducted (Fig. S23, ESI,† Fig. 4b). The adsorption energy of intermediate Cl* (ΔE_{Cl^*}) on $Pt_3Ni_{2-3x}@(Ni_3B)_x$ is 0.09 eV, which is more positive than the ΔE_{Cl^*} of the Pt_3Ni networks (−0.11 eV), indicating the better Cl^- resistance. Moreover, the more negative water adsorption energy ($\Delta E_{H_2O^*}$ = −0.69 eV) further decreased the Cl^-

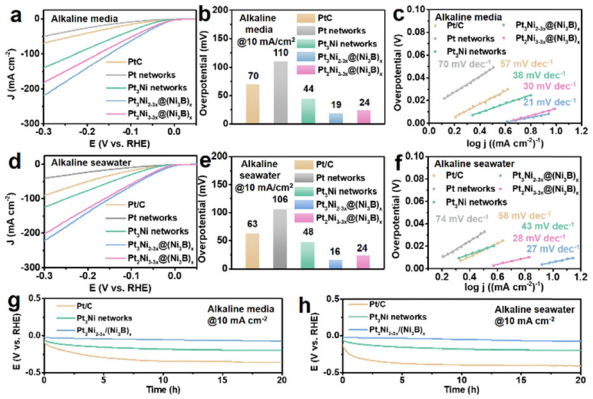


Fig. 3 Respective HER polarization curves, overpotentials (at current density of 10 mA cm^{-2}), and Tafel plots of the Pt/C, Pt networks, Pt_3Ni networks, $Pt_3Ni_{2-3x}@(Ni_3B)_x$, and $Pt_2Ni_{3-3x}@(Ni_3B)_x$ in (a)–(c) alkaline media and (d)–(f) alkaline seawater. Chronopotentiometry of the Pt/C, Pt_3Ni networks and $Pt_3Ni_{2-3x}@(Ni_3B)_x$ under the current density of 10 mA cm^{-2} in (g) alkaline media and (h) alkaline seawater.

 This journal is © The Royal Society of Chemistry 2025

Published on 06 December 2024. Downloaded by University of the Witwatersrand on 7/30/2025 2:13:24 PM.

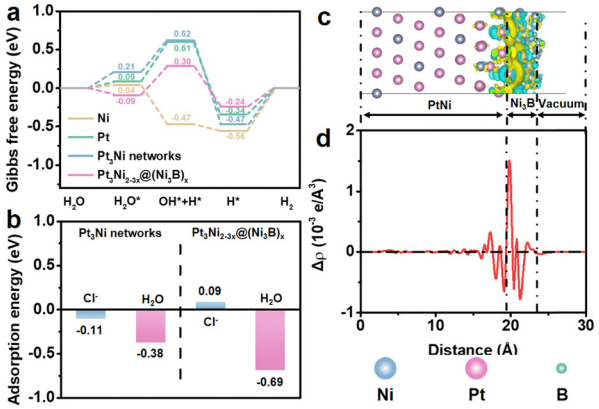


Fig. 4 Calculated adsorption free energy diagram for (a) the progress of the HER and (b) the comparison of Cl^- and H_2O. (c) Differential charge density diagrams (the blue region represents electron depletion; the yellow region represents electron accumulation) and (d) planar-average charge density along the *z*-direction (across the heterojunction) of $Pt_3Ni_{2-3x}@(Ni_3B)_x$.

adsorption during the competitive adsorption between water and Cl^-. To have a more detailed understanding of the electronic properties of the $Pt_3Ni_{2-3x}@(Ni_3B)_x$, we plot in Fig. 4c the differential charge density diagrams calculated from the model of $Pt_3Ni_{2-3x}@(Ni_3B)_x$. It is clear that the introduction of the Ni_3B nanolayers has enhanced the asymmetric charge transfer, leading to charge polarization and electron redistribution on the interface, in which PtNi and Ni_3B act as electron donor and acceptor, respectively. Fig. 4d shows the plane-averaged charge density along the *z*-direction (across the heterojunction). The charge density around the heterojunction is no longer equivalent and remarkable charge rearrangement occurs around the interface and electrons have transferred from PtNi to Ni_3B. The partial density of states diagrams also show the electronic structures (see Fig. S24 and a detailed description, ESI†).

In summary, we have presented the fabrication of a heterophase catalyst composed of PtNi networks coated with Ni_3B. Owing to the gap in the work function, a directed electron transfer from a crystalline PtNi to Ni_3B coating was facilitated. As a result, $Pt_3Ni_{2-3x}@(Ni_3B)_x$ demonstrates both superior activity and Cl^- resistance. Experimental results combined with the theoretical calculations disclosed that the excellent alkaline HER activity of $Pt_3Ni_{2-3x}@(Ni_3B)_x$ can be attributed to the electron-rich surface of the Ni_3B nanolayers, which effectively increases the hydrogen adsorption–desorption kinetics and mitigates corrosion promoted by Cl^-.

This study was supported by the National Key Research and Development Program of China (2022YFB3805600, 2022YFB 3805604), National Natural Science Foundation of China (52201286) National 111 project (B20002), Key R&D Program of Shandong Province, China (2023CXGC010314), and Guangdong Basic and Applied Basic Research Foundation (2021A15 15111131, 2022A1515011905, 2024A1515012613). We thank the Nanostructure Research Centre (NRC) for performing the S/TEM imaging, Hubei Provincial Natural Science Foundation of China (2024AFB195), and South Africa's National Research Foundation through the SARChI Chair in Materials Electrochemistry and Energy Technologies (MEET) (132739).

Data availability

The data supporting this article have been included as part of the ESI.†

Conflicts of interest

There are no conflicts to declare.

Notes and references

1 Y.-X. Xiao, J. Ying, J.-B. Chen, X. Yang, G. Tian, J.-H. Li, C. Janiak and X.-Y. Yang, *Adv. Funct. Mater.*, 2024, 2418264.
2 Y.-Y. Ma, C.-X. Wu, X.-J. Feng, H.-Q. Tan, L.-K. Yan, Y. Liu, Z.-H. Kang, E.-B. Wang and Y.-G. Li, *Energy Environ. Sci.*, 2017, **10**, 788–798.
3 Y.-X. Xiao, J. Ying, J.-B. Chen, Y. Dong, X. Yang, G. Tian, J. Wu, C. Janiak, K. I. Ozoemena and X.-Y. Yang, *Chem. Mater.*, 2022, **34**, 3705–3714.
4 Y.-X. Xiao, J. Ying, G. Tian, X. Q. Zhang, C. Janiak, K. I. Ozoemena and X.-Y. Yang, *Chem. Commun.*, 2021, **57**, 986–989.
5 F.-F. Pu, Y.-X. Xiao, X. Yang, F. Yu, L. Xia, J.-B. Chen, L. Wu, J.-J. Xie, W.-Y. Zhao, Y. Liu, L.-Y. Wang, J. Ying, M.-J. Liao, K. I. Ozoemena, G. Tian, F. Wang and X.-Y. Yang, *Chem. Eng. J.*, 2023, **474**, 145630.
6 X.-Q. Zhang, Y.-X. Xiao, G. Tian, X. Yang, Y. Dong, F. Zhang and X.-Y. Yang, *Chem. Eng. J.*, 2023, **29**, e202202811.
7 Y. Kuang, M. J. Kenney, Y. T. Meng, W. H. Hung, Y. J. Liu, J. E. Huang, R. Prasanna, P. S. Li, Y. P. Li, L. Wang, M. C. Lin, M. D. McGehee, X. M. Sun and H. J. Dai, *Proc. Natl. Acad. Sci. U. S. A.*, 2019, **116**, 6624–6629.
8 X. Yang, Y.-X. Xiao, J.-B. Chen, F. Yu, G. Tian, F.-F. Pu, S. Zhang, S. I. C. de Torresi, M. D. Symes, C. Janiak and X.-Y. Yang, *Sci. China Mater.*, 2023, **66**, 3887–3894.
9 F. Yu, Y.-X. Xiao, J.-B. Chen, G. Tian, X. Yang, F.-F. Pu, J.-Y. Ouyang, K. I. Ozoemena, M. D. Symes, R. M. Torresi, F. Wang and X.-Y. Yang, *Chem. Mater.*, 2023, **35**, 8529–8539.
10 S. Zhang, Y. Wang, S. Li, Z. Wang, H. Chen, L. Yi, X. Chen, Q. Yang, W. Xu, A. Wang and Z. Lu, *Nat. Commun.*, 2023, **14**, 4822.
11 Y.-X. Xiao, J. Ying, H. W. Liu and X.-Y. Yang, *Front. Chem. Sci. Eng.*, 2023, **17**, 1677–1697.
12 A. Saad, Y. Gao, K. A. Owusu, W. Liu, Y. Wu, A. Ramiere, H. Guo, P. Tsiakaras and X. Cai, *Small*, 2022, **18**, e2104303.
13 X. Han, L. Zhao, Y. Liang, J. Wang, Y. Long, Z. Zhou, Y. Zhang, Y. Li and J. Ma, *Adv. Energy Mater.*, 2022, **12**, 2202747.
14 R. Gumeniuk, H. Borrmann, A. Leithe-Jasper and Z. Kristallogr, *NCS*, 2006, **221**, 425–426.
15 D. He, L. Zhang, D. He, G. Zhou, Y. Lin, Z. Deng, X. Hong, Y. Wu, C. Chen and Y. Li, *Nat. Commun.*, 2016, **7**, 12362.
16 H.-C. Lee, B. M. Kim, C. K. Jeong, R. Toyoshima, H. Kondoh, T. Shimada, K. Mase, B. Mao, Z. Liu, H. Lee, C.-Q. Huang, W. X. Li, P. N. Ross and B. S. Mun, *Catal. Today*, 2016, **260**, 3–7.
17 F. Tao, M. E. Grass, Y. W. Zhang, D. R. Butcher, J. R. Renzas, Z. Liu, J. Y. Chung, B. S. Mun, M. Salmeron and G. A. Somorjai, *Science*, 2008, **322**, 932–934.
18 W. Cui, W. An, L. Liu, J. Hu and Y. Liang, *J. Hazard. Mater.*, 2014, **280**, 417–427.
19 Y.-X. Xiao, J. Ying, G. Tian, X. Yang, Y. X. Zhang, J. B. Chen, Y. Wang, M. D. Symes, K. I. Ozoemena, J. Wu and X. Y. Yang, *Nano Lett.*, 2021, **21**, 7870–7878.
20 W.-J. Jiang, S. Niu, T. Tang, Q.-H. Zhang, X.-Z. Liu, Y. Zhang, Y.-Y. Chen, J.-H. Li, L. Gu, L.-J. Wan and J.-S. Hu, *Angew. Chem., Int. Ed.*, 2017, **56**, 6572–6577.
21 P.-Z. Chen, K. Xu, T.-P. Zhou, Y. Tong, J.-C. Wu, H. Cheng, X.-L. Lu, H. Ding, C.-Z. Wu and Y. Xie, *Angew. Chem., Int. Ed.*, 2016, **128**, 2534–2538.
22 J. Fang, H. Fan, M. Li and C. Long, *J. Mater. Chem. A*, 2015, **3**, 13819–13826.
23 Y.-X. Xiao, J. Ying, G. Tian, Y. Tao, H. Wei, S.-Y. Fan, Z.-H. Sun, W.-J. Zou, J. Hu, G.-G. Chang, W. Li, X.-Y. Yang and C. Janiak, *Appl. Catal., B*, 2019, **259**, 118080.
24 V. M. Nikolic, S. Lj Maslovara, G. S. Tasic, T. P. Brdaric, P. Z. Lausevic, B. B. Radak and M. P. M. Kaninski, *Appl. Catal. B*, 2015, **179**, 88–94.
25 Y. Zheng, Y. Jiao, M. Jaroniec and S. Z. Qiao, *Angew. Chem., Int. Ed.*, 2015, **54**, 52–65.